water

MDPI

Article

Abundant Precipitation in Qilian Mountains Generated from the Recycled Moisture over the Adjacent Arid Hexi Corridor, Northwest China

Zhihua Zhang [1,2], Qiudong Zhao [3,4] and Shiqiang Zhang [1,2,*]

1 Shaanxi Key Laboratory of Earth Surface System and Environmental Carrying Capacity, Northwest University, Xi'an 710127, China; NWU_zhihuazhang@163.com
2 College of Urban and Environmental Science, Northwest University, Xi'an 710127, China
3 State Key Laboratory of Cryospheric Sciences, Cold and Arid Regions Environmental and Engineering Research Institute, Chinese Academy Sciences, Lanzhou 730000, China; dsslab@163.com
4 Key Laboratory of Ecohydrology of Inland River Basin, Chinese Academy Sciences, Lanzhou 730000, China
* Correspondence: zhangsq@nwu.edu.cn; Tel.: +86-02988308427

Abstract: The observed precipitation was suggestive of abundant precipitation in upstream Qilian mountains and low precipitation in the downstream oasis and desert in an endorheic basin. However, precipitation in mountains generated from the recycled moisture over oasis and desert areas has rarely been studied. The climatological patterns of water vapor from 1980 to 2017 in the Qilian Mountain Region (QMR) and Hexi Corridor Region (HCR) were investigated by the European Centre for Medium-Range Weather Forecasts Interim reanalysis dataset and the Modern-Era Retrospective Analysis for Research and Application, Version 2 reanalysis dataset. The results suggest that the precipitable water content decreases from the adjacent to the mountain areas. There are two channels that transport water vapor from the HCR to the QMR in the low troposphere (surface—600 hPa), suggesting that parts of recycled moisture generated from evapotranspiration over the oasis and desert of the HCR is transported to the QMR, contributing to the abundant precipitation in the QMR. This indicates that the transport mechanism is probably because of the "cold and wet island effect" of the cryosphere in QMR. This is likely one of the essential mechanisms of the water cycle in endorheic river basins, which has rarely been reported.

Keywords: precipitation generation; recycled moisture; water vapor; channel; Qilian Mountain Region; Hexi Corridor Region

Citation: Zhang, Z.; Zhao, Q.; Zhang, S. Abundant Precipitation in Qilian Mountains Generated from the Recycled Moisture over the Adjacent Arid Hexi Corridor, Northwest China. *Water* **2021**, *13*, 3354. https://doi.org/10.3390/w13233354

Academic Editor: Momcilo Markus

Received: 31 October 2021
Accepted: 23 November 2021
Published: 26 November 2021

1. Introduction

Arid and semiarid areas are the regions most sensitive to global climate changes owing to the scarcity of water resources and vulnerable ecosystems [1], especially when considering larger precipitation variations [2,3]. As part of the ancient Silk Road in northwestern China, the Hexi Corridor Region (HCR) is a typical arid area, including oases and deserts of endorheic basins. On the other hand, the adjacent Qilian Mountains Region (QMR) is part of the eastern area of the Tibetan Plateau (TP), which provides the HCR with water for life, agriculture, and industry. It is called the "water tower" of the HCR [4].

Wang et al. [5] suggested that the alpine permafrost-snow-ice zone with an altitude greater than 3600 m a.s.l. generates 80.2% of the annual total mountainous runoff using stable isotopes. The Qilian Mountain and Hexi Corridor Region (QM-HCR) has clear vertical landscape zones of glacial-snow/permafrost, meadow, forest, cropland, and the Gobi Desert from high to low altitudes (Figure 1). The QMR is mainly covered with ice-snow-permafrost, alpine cold desert zones, and meadows. In contrast, the HCR is primarily covered with forest, cropland, and the vast Gobi Desert, a common pattern in endorheic river basins in China. The QMR and HCR show significant differences in terms of precipitation and evaporation. For example, Chen and Han [6] reported that

the alpine cold desert zone at 4000–5000 m a.s.l. has plentiful precipitation and low evapotranspiration. Zhang et al. [7] reported that the annual precipitation gradient is approximately 12 mm/100 m in the upper reach of Shule River Basin (above 3000 m a.s.l.), indicating that the glacier and alpine cold desert zone have the highest precipitation. He et al. [8] reported that the forests above 2700 m a.s.l. exhibited higher evaporation from 2003 to 2008. Gao et al. [9] suggested that the water resource loss of evapotranspiration within croplands and forests is up to 25.69 × 10^8 m^3 and accounts for 41% of the net water consumption in the HCR.

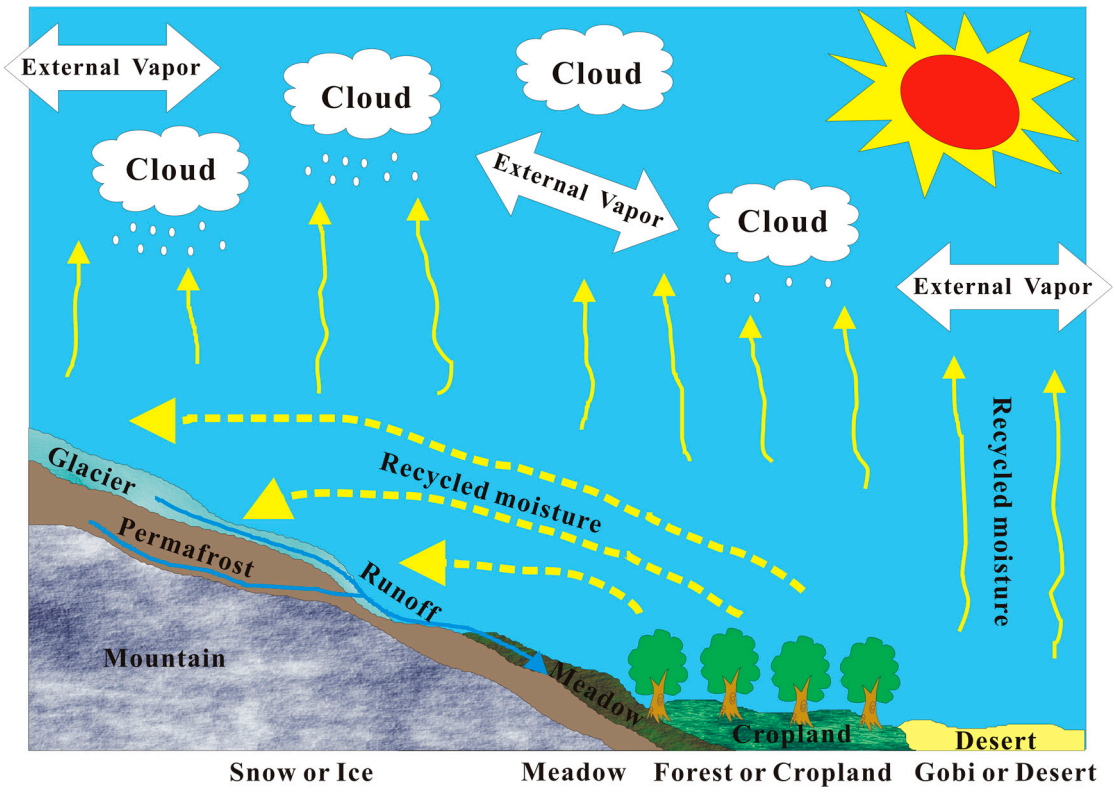

Figure 1. The schematic diagram of the atmospheric water vapor cycle including external water vapor and recycled moisture.

The above studies suggest that most of the precipitation in forests and croplands in HCR are converted into evapotranspiration. As the primary water resources for the entire endorheic river basin, glacier and alpine cold desert zones have the most abundant precipitation and low evaporation (sublimation). However, a possible link between the high precipitation in QMR and strong evapotranspiration over HCR has rarely been addressed. Moreover, forests, croplands, meadows, glaciers, and permafrost are predicted to change under future climate change conditions (such as the 1.5 and 2 °C global warming scenarios under the Paris Agreement). Therefore, understanding the water cycle mechanism between different regions/landscapes in the QM-HCR is critical for local water resource management.

Atmospheric water vapor is an essential material basis for precipitation formation, and its transportation is the most frequent process in the atmospheric water cycle [10]. The typical definition of precipitating vapor is a mixture of advection vapor, transpiration vapor, and surface evaporation vapor; the latter two are called typical recycled moisture. The terrestrial moisture recycling by evapotranspiration has been recognized as an important source of precipitation. The isohyets and the vegetation belts have similar patterns, while the different land use/land cover has varied recycling of moisture; there exists an important feedback mechanism between land use and climate [11], the vegetation probably influences the local rainfall amount. Rainfall is always the result of the cooling of air masses through

an uplift. The two most important mechanisms include the rise of unstable pockets of air (thunderstorms) and the orographic effect where air is forced up over the slope by advection.

Some studies have produced many interesting results in atmospheric moisture transport and its relationship with precipitation on TP. Ma et al. [12] reviewed the atmospheric moisture transport and associated circulation patterns in TP; they suggested that quantifying the contribution of atmospheric water vapor from the surrounding sources as well as the local moisture recycling on the TP's precipitation is one of direction of research. Chen et al. [13] developed a climatology of origin (destination) of air mass and moisture transported to (from) the TP using a Lagrangian moisture diagnosis combined with the forward and backward atmospheric tracking schemes, which suggested that the dominant origin of the moisture supplied to the TP is a narrow tropical-subtropical band in the extended Arabian Sea from the Indian subcontinent to the Southern Hemisphere. Zhang et al. [14] suggested that the enhanced water vapor transport from the Indian Ocean during July and September and the intensified local hydrological recycling seem to be the primary reasons behind the recent precipitation increase over the TP. Ma et al. [15] suggested that the summer precipitation extremes in the southeast TP absorb about 75% of total moisture from the Bay of Bangla. In short, these studies mainly focus on the source and moisture recycling at large scales such as TP, and the relatively small scales, such as QM-HCR, have been little reported.

The QMR and HCR are far away from the ocean, and the contribution of local recycled moisture may explain the abundant precipitation in QMR and the low precipitation in HCR. For example, Zhao et al. [16] reported that the contribution of recycled moisture to precipitation in the upper, middle, and lower reaches of the Heihe Basin is approximately 52.4%, 56.5%, and 21.4% by isotope tracing, respectively; the Heihe Basin is part of the QM-HCR. However, there is large potential evapotranspiration over the HCR having low precipitation, indicating that part of the recycled moisture generated from evapotranspiration was transported to other regions. In contrast, there is less evapotranspiration over the glacier and alpine cold desert zone, which indicates that the local moisture recycling contributed to the local precipitation in the QMR on a limited basis. The more plentiful rainfall in the QMR in comparison to the HCR is difficult to explain by only considering the traditional local moisture recycling process.

Ding and Zhang [17] proposed a new hypothesis for the water cycle over different regions of the endorheic basin. They believed that part of the recycled moisture generated from the evapotranspiration of forest zones and croplands in the downstream oasis contributed to local precipitation as well as transport to the mountainous areas. Further, both the visible water vapor and horizontal transport of recycled moisture can lead to abundant rainfall in the glacier and alpine cold desert zones (Figure 1). However, interdisciplinary research between hydrology and atmosphere science on the transport of recycled moisture between different adjacent regions in the endorheic basin has rarely been addressed in the literature. Additionally, the observation and quantification of recycled moisture transport still pose significant challenges because they span the fields of atmospheric science, hydrology, geography, and geology [17]. The climatological pattern of the water vapor transport flux in the QM-HCR likely provides clues for testing the hypothesis.

The vertical vapor transport process links water vapor between the low and high troposphere and the horizontal water vapor transport process leads to the spatial distribution of water vapor and precipitation [18]. Reanalysis datasets are powerful tools to analyze water vapor transport. Thus, a preliminary study on water vapor transport in the QM-HCR based on reanalysis datasets and in-situ precipitation data was conducted.

Several global and long-term gridded atmospheric reanalysis datasets have been developed and used for investigating regional climate variations and predictions. These include the National Centers for Environmental Prediction (NCEP) reanalysis, National Aeronautics and Space Administration (NASA), and Modern-Era Retrospective Analysis for Research and Application (MERRA) datasets. The European Centre for Medium-

Range Weather Forecasts (ECMWF) Interim reanalysis datasets (ERA-Interim) have also been developed and are popular for analyzing global climate and water vapor [19,20]. Simmons et al. [21] reported on the quality of ERA-Interim near-surface field datasets by comparing field observations with climatic data records. Decker et al. [22] confirmed that the land surface evaporation of ERA-Interim compared favorably with the flux tower observations and other reanalysis datasets. Some studies [20,23] suggest that the ERA-Interim and MERRA can better represent water vapor transport characteristics in the Tibetan Plateau and surrounding regions. The latest comparative experiments also report that the fifth-generation ECMWF atmospheric reanalysis (ERA5) dataset and MERRA-2 are more suitable for studying the atmospheric precipitable water content (PWC) in Central Asia [24]. Gelaro et al. [25] suggested that MERRA-2 is an improvement on MERRA because of its relatively high resolution ($0.5^\circ \times 0.625^\circ$). The spatial resolution of NCEP is only $2.5^\circ \times 2.5^\circ$ [20] with a small number of grids in the QM-HCR; this limits the detailed delineation of water vapor. Thus, the ERA-Interim and MERRA-2 are selected as the reanalysis datasets in the study.

Several studies on water vapor have been conducted in the QM-HCR and surrounding areas, including the estimation of water vapor transport characteristics (e.g., [16]), variations in water vapor variables, for example, [26,27], and the relationship between water vapor and precipitation variations, for example, [20,28]. However, few studies have focused on the transport of recycled moisture between the QMR and the HCR via the water cycle. Our study attempts to understand the regional water vapor transport process by analyzing the water vapor climatological patterns based on ERA-Interim, MERRA-2, and observed precipitation data. The objectives include: (1) to analyze the spatial pattern of water vapor climatology in the QM-HCR for the 1980–2017 wet season (May–September), dry season (October–April) and on an annual basis; and (2) to identify the transport channels for recycled moisture and discuss their implications for water recycling in the QM-HCR.

2. Data and Methods

2.1. Study Area

The QM-HCR is in the hinterland of Eurasia on the northeastern edge of the Tibetan Plateau. The HCR has an arid climate with an annual precipitation of less than 200 mm [29]. On the other hand, the annual rainfall can reach 400–700 mm in the QMR, which is much more than that in the HCR.

The information about the meteorological stations in and around the QM-HCR is listed in Table 1. Based on the observation data of stations and the ordinary kriging interpolation method [30], the spatial distribution of average annual precipitation in the QM-HCR in 1980–2017 (not shown here) suggests that the rainfall gradually decreases from the southeast to the northwest, especially in the QMR. The maximum precipitation is 527.2 mm at the MY station, and the minimum is 16.3 mm at the LH station. The average annual precipitation during 1980 to 2017 is 182.0 mm, it is 154.7 mm (85%) in the wet season, while it is 27.3 mm (15%) in the dry season in QM-HCR.

Table 1. Information on the meteorological stations in and around the QM-HCR.

Station ID	Latitude	Longitude	Full Name	Abbreviation	Station ID	Latitude	Longitude	Full Name	Abbreviation
52203	42.82	93.52	Hami	HM	52679	37.92	102.67	Wuwei	WW
52267	41.95	101.07	Mesozoic-Cenozoic	MC	52681	38.63	103.08	Minqin	MQ
52313	41.53	94.67	Hongliuhe	HLH	52707	36.80	93.68	Xiaozaohuo	XZH
52323	41.80	97.03	Mazongshan	MZS	52713	37.85	95.37	Dachaidan	DCD
52343	41.93	99.90	Jihede	JHD	52737	37.37	97.37	Delingha	DLH
52378	41.37	102.37	Guaizihu	GZH	52754	37.33	100.13	Gangcha	GC
52418	40.15	94.68	Dunhuang	DH	52765	37.38	101.62	Menyuan	MY

Table 1. *Cont.*

Station ID	Latitude	Longitude	Full Name	Abbreviation	Station ID	Latitude	Longitude	Full Name	Abbreviation
52424	40.53	95.77	Anxi	AX	52787	37.20	102.87	Wushaoling	WSL
52436	40.27	97.03	Yumenzhen	YMZ	52788	37.12	103.50	Songshan	SS
52441	40.72	98.62	Wutonggou	WTG	52797	37.18	104.05	Jingtai	JT
52446	40.30	99.52	Dingxin	DX	52818	36.42	94.90	Geermu	GEM
52447	40.00	98.90	Jinta	JTa	52825	36.43	96.42	Nuomuhong	NMH
52533	39.77	98.48	Jiuquan	JQ	52833	36.92	98.48	Wulan	WL
52546	39.37	99.83	Gaotai	GT	52836	36.30	98.10	Dulan	DL
52576	39.22	101.68	Alxa League	AL	52842	36.78	99.08	Chaka	CK
52602	38.75	93.33	Lenghu	LH	52856	36.27	100.62	Qabqa	QBQ
52633	38.80	98.42	Tuole	TL	52866	36.72	101.75	Xining	XN
52645	38.42	99.58	Yeniugou	YNG	52868	36.03	101.43	Guide	GD
52652	38.93	100.43	Zhangye	ZY	52876	36.32	102.85	Minhe	MH
52657	38.18	100.25	Qilian	QL	52884	36.35	103.93	Gaolan	GL
52661	38.80	101.08	Shandan	SD	52889	36.05	103.88	Lanzhou	LZ
52674	35.87	104.15	Yongchang	YC	52983	38.23	101.97	Yuzhong	YZ

The minimum enclosed rectangle (hereafter referred to as box; Miao et al. [31]) of the QM-HCR (35.79°–42.85° N, 92.75°–104.30° E; Figure 2) is used to calculate and analyze the boundary and regional net water vapor flux.

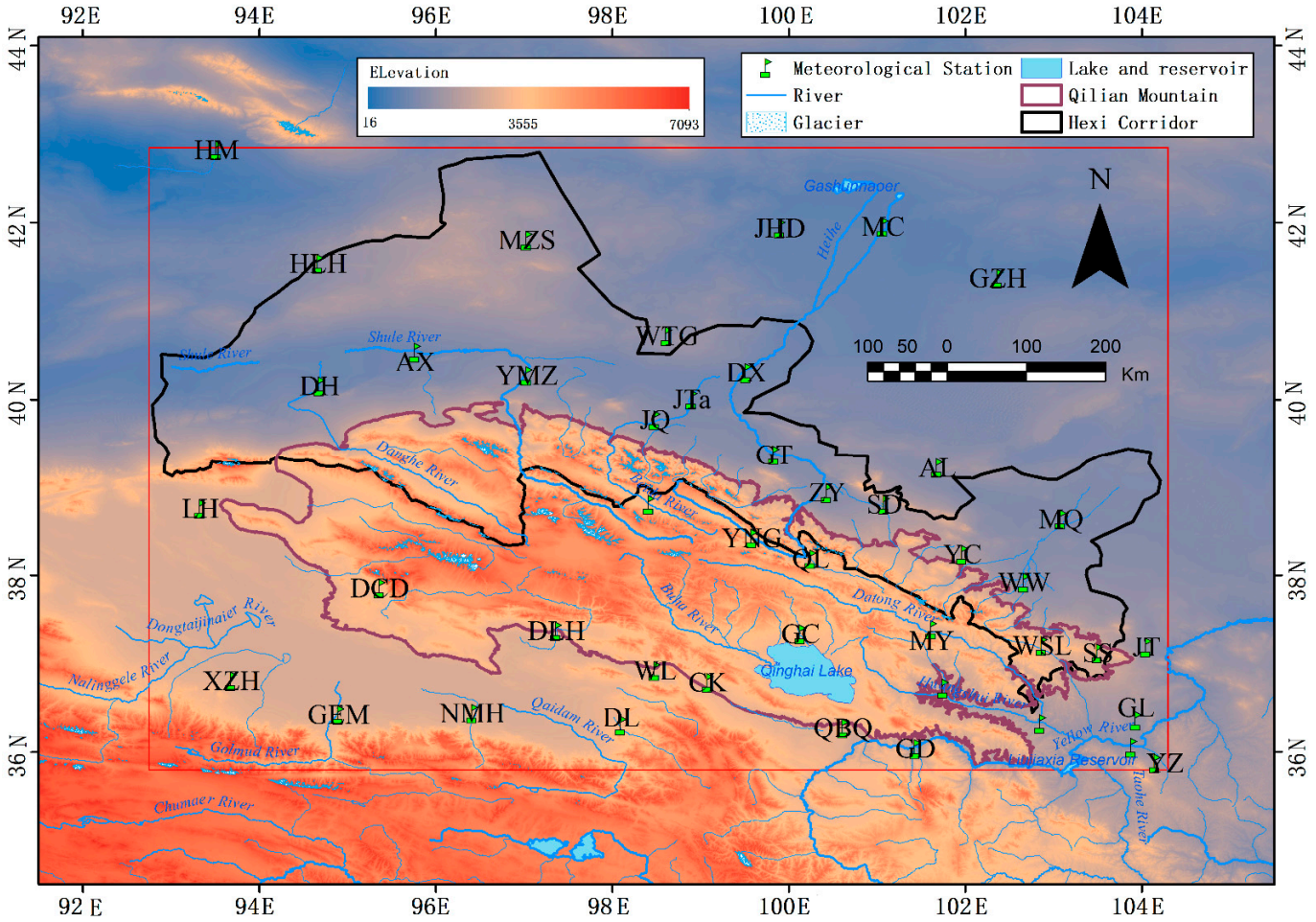

Figure 2. The distribution of the meteorological stations, glaciers and rivers in the QM-HCR; the red box is the minimum enclosed rectangle of the QM-HCR.

2.2. Data

The monthly precipitation data from 44 Chinese national meteorological stations for 1980–2017 were obtained from the China Meteorological Data website (http://data.cma.cn, accessed on 12 October 2018). They were initially observed twice daily at 8:00 a.m. and 20:00 p.m. (Chinese Standard Time) at the standard meteorological station. Quality control

was ensured by the National Climate Center of the China Meteorological Administration (NCC/CMA). The observed in-situ precipitation was used to validate data from ERA-Interim and MERRA-2 datasets.

ERA-Interim is a global atmospheric reanalysis product that covered the modern satellite era from January 1979, developed by the ECMWF, and is continuously updated in real time [32]. The system analyzes the global surface changes by combining them with initial data from the Integrated Forecast System (IFS) in a 12-h analysis window. The original spatial resolution of the dataset is approximately 80 km (T255 spectral resolution) on 60 vertical levels from the surface up to 0.1 hPa, and was then interpolated to multiple resolutions (up to 0.125° × 0.125°). The ERA-Interim atmospheric reanalysis is built upon consistent assimilation of an extensive set of observations, including satellite remote sensing, in-situ, profiler data, radio soundings, and other observations distributed worldwide. The short-range forecasts (first-guess fields), which are the data assimilation results, are close to the atmospheric observations. The use of ERA-Interim has indicated that moisture estimates at the lowest model level are generally of high quality in the 0–12 h forecast range [16]. The ECMWF checked the data quality before it was released; they controlled for the initial model inputs, observations, output data and assimilation schemes, and variables. ERA-Interim data were downloaded from the website (https://www.ecmwf.int/en/forecasts/dataset/ecmwf-reanalysis-interim, accessed on 10 September 2020).

MERRA-2 is the latest atmospheric reanalysis dataset from the satellite era produced by the Global Modeling and Assimilation Office (GMAO) of NASA [25]. The MERRA-2 is obtained by the Goddard Earth Observing System Model Version 5 (GEOS-5) with its Atmospheric Data Assimilation System (ADAS) Version 5.12.4. MERRA-2 data cover the period from 1980 to the present using a temporal resolution less than 6 h. Two-dimensional diagnostics (surface fluxes, radiation, and single-level meteorology) are produced at 1-h intervals. Additionally, the 3-h three-dimensional atmospheric products at a spatial resolution of 0.5° latitude × 0.625° longitude are also available. GMAO has already implemented various data quality controls for MERRA-2, mainly including the preprocessing of NO-DATA, restrictions on model input data, observed data, output data, assimilation scheme, and variables and assimilated channels of sensors. The real-time updated MERRA-2 reanalysis dataset can be downloaded from the website (https://disc.gsfc.nasa.gov, accessed on 12 October 2018).

The monthly averages of reanalysis variables in 1980–2017 were downloaded and then extracted by the QM-HCR box. The synoptic monthly means are the monthly average at each analysis time (00, 06, 12, and 18 UTC), and monthly Means Accumulations are the Monthly Means of Daily Means but are for accumulated fields (e.g., precipitation, radiation) [25,32]. The data included precipitation (pre), evaporation (evap), surface pressure (sp), specific humidity (q), and longitudinal (v), and latitudinal wind speed (u) at 1000–200 hPa for ERA-Interim (0.125° × 0.125°) and MERRA-2 (0.5° × 0.625°). The water vapor flux was calculated using ERA-Interim and MERRA-2 datasets.

To further control the data quality of precipitation from ERA-Interim and MERRA-2 in the QM-HCR, comparisons of regional average precipitation between in-situ observation and that from MERRA-2 (Figure 3a) and ERA-Interim (Figure 3b) suggested that the scatter points are evenly distributed on both sides of the 1:1 line, which indicated that in-situ observation was equal to that observed from reanalysis data. The values for the square of Pearson (ordinary) Coefficient of correlation (R^2) and Absolute Mean Error (AME) of the regional monthly precipitation are 0.92 and 3.1 mm for MERRA-2 and 0.89 and 3.5 mm for ERA-Interim, respectively. These precipitation rates indicate that the monthly precipitation from MERRA-2 and ERA-Interim are closely correlated with observations. Moreover, the monthly precipitation from two reanalysis datasets and observations exhibit a consistent seasonal pattern (unimodal type; not shown here). The rainfall is mainly concentrated in the wet season (156.6 mm), which accounts for 85% of the annual precipitation (184.9 mm)

in 1980–2017. The rainfall comparisons indicate that the ERA-Interim and MERRA-2 can be used to analyze water vapor transport characteristics in the QM-HCR.

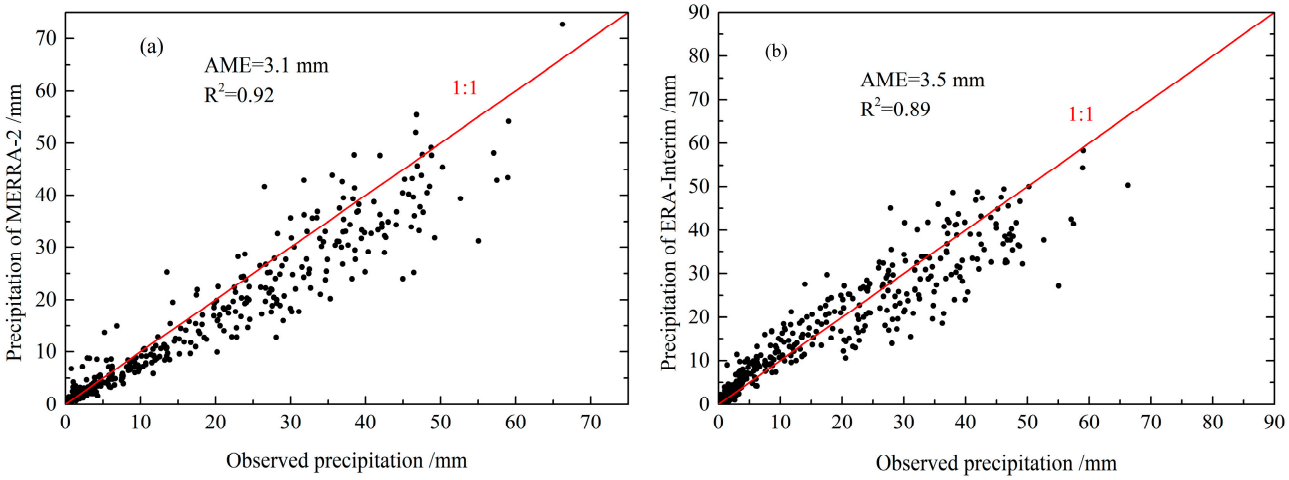

Figure 3. Scatter plot between observed monthly precipitation and precipitation from MERRA-2 (**a**) and ERA-Interim (**b**) in the QM-HCR.

2.3. Methods

The water vapor flux, flux divergence, boundary, regional net water vapor flux, and atmospheric PWC were calculated based on ERA-Interim and MERRA-2. The data were then processed using the Grid Analysis and Display System (GrADS) software developed by the Center for Ocean-Land-Atmosphere Studies (COLA), George Mason University. A simple statistical method (Pearson correlation coefficient) was used to analyze the relationship between external water vapor, recycled moisture, and observed precipitation.

Water vapor flux represents the amount of water vapor flowing through a unit area in unit time and is categorized as horizontal and vertical water vapor flux. The horizontal water vapor flux (Q) was calculated by Equation (1) [33]:

$$Q = -\frac{1}{g}\int_{p_s}^{p_l} qVd_p, \tag{1}$$

where V represents the wind speed, which is divided into wind speed at longitudinal and latitudinal directions with units of m/s; g represents the gravity acceleration by 9.8 m/s^2; and p_l is the top pressure. Given that the specific humidity above 200 hPa is nearly 0 in the QM-HCR, p_l is considered to be 200 hPa, which is different from the 300 hPa used in some studies [34,35]. Here, p_s is the surface pressure. The horizontal water vapor flux includes longitudinal (q_v) and latitudinal water vapor flux (q_u). These factors are calculated in Equations (2) and (3) [33], respectively.

$$q_v = -\frac{1}{g}\int_{p_s}^{p_l} qvd_p \tag{2}$$

$$q_u = -\frac{1}{g}\int_{p_s}^{p_l} qud_p. \tag{3}$$

The water vapor flux divergence (Q_{div}) and PWC are calculated using Equations (4) and (5) [35], respectively:

$$Q_{div} = -\frac{1}{g}\int_{p_s}^{p_l} \Delta(qV)d_p \tag{4}$$

$$PWC = -\frac{1}{g}\int_{p_s}^{p_l} qd_p. \tag{5}$$

The regional net water vapor flux (Δq) refers to the difference between the water vapor input and the atmospheric output at a specific time. Generally, this is calculated using the "Box model" [31]. The Δq of the QM-HCR (the red box in Figure 2) was calculated as follows. For ERA-Interim and MERRA-2, the positive direction ($\Delta q > 0$) of Δq is "from west to east" and "from south to north," respectively. The water vapor flux at the four boundaries (Δq_{v_North}), (Δq_{v_South}), (Δq_{u_West}), and (Δq_{u_East}) was calculated from Equations (6)–(9), respectively [20,31]:

$$\Delta q_{v\_North} = -\int_{\lrcorner_{west}}^{\lrcorner_{east}} q_{v\_north} a \cos \varphi_{north} d\lrcorner \quad (6)$$

$$\Delta q_{v\_South} = \int_{\lrcorner_{west}}^{\lrcorner_{east}} q_{v\_south} a \cos \varphi_{south} d\lrcorner \quad (7)$$

$$\Delta q_{u\_West} = \int_{\varphi_{north}}^{\varphi_{south}} q_{u\_west} a d_{\varphi} \quad (8)$$

$$\Delta q_{u\_East} = -\int_{\varphi_{north}}^{\varphi_{south}} q_{u\_east} a d_{\varphi}. \quad (9)$$

The regional net water vapor flux (Δq) is calculated by Equation (10):

$$\Delta q = \Delta q_{v\_North} + \Delta q_{v\_South} + \Delta q_{u\_West} + \Delta q_{u_{East}}. \quad (10)$$

In this study, the surface pressure (unit: hPa) of each grid is extracted from two reanalysis datasets. Here, q is the specific humidity of each pressure layer with units of kg/kg; a is the mean radius of the earth at 6.371×10^3 km; φ and λ are the latitude and longitude, respectively; q_{u_east} and q_{u_west} are the water vapor flux (q_u) at the east, and west boundaries, respectively; q_{v_south} and q_{v_north} are the water vapor flux (q_v) at the south and north boundary, respectively; φ_{north} and φ_{south} represent the latitudes of the north and south edge, respectively; and $\lrcorner_{east}$ and $\lrcorner_{west}$ represent the longitudes of the east and west boundaries, respectively.

3. Results

3.1. Atmospheric Precipitable Water Content

The spatial pattern of atmospheric PWC climatology during the annual (Figure 4a,d), wet (Figure 4b,e) and dry seasons (Figure 4c,f) were calculated using ERA-Interim and MERRA-2. The spatial patterns of climatology derived from the two reanalysis datasets are similar. However, considering the higher spatial resolution of ERA-Interim than that of MERRA-2, we used ERA-Interim to analyze the spatial pattern of other variables.

There is higher atmospheric PWC in the southeastern, eastern, northern, and northwestern QM-HCR. In contrast, lower water content is determined in the alpine areas of the QMR. The water content decreases from the surrounding areas to the high-altitude mountains and is negatively correlated with altitude (Figure 4). The average atmospheric PWC is 6.93 mm annually, and the average content during the wet season (11.63 mm, Figure 4b,e) is higher than that of the dry season (3.54 mm, Figure 4c,f). This demonstrates a distinct unimodal type pattern, which is consistent with the seasonal pattern of observed precipitation.

3.2. Water Vapor Flux and Water Vapor Flux Divergence

The spatial patterns of column-integrated water vapor flux and the climatology of water vapor flux divergence during the annual (Figure 5a) wet (Figure 5b) and dry seasons (Figure 5c) from 1980 to 2017 in the QM-HCR suggest that northwesterly and westerly wind control the water vapor during all seasons. The regional average water vapor flux is the greatest in the wet season, followed by annual values. These values are the weakest in the dry season, proving that the annual precipitation is mainly concentrated in the wet season.

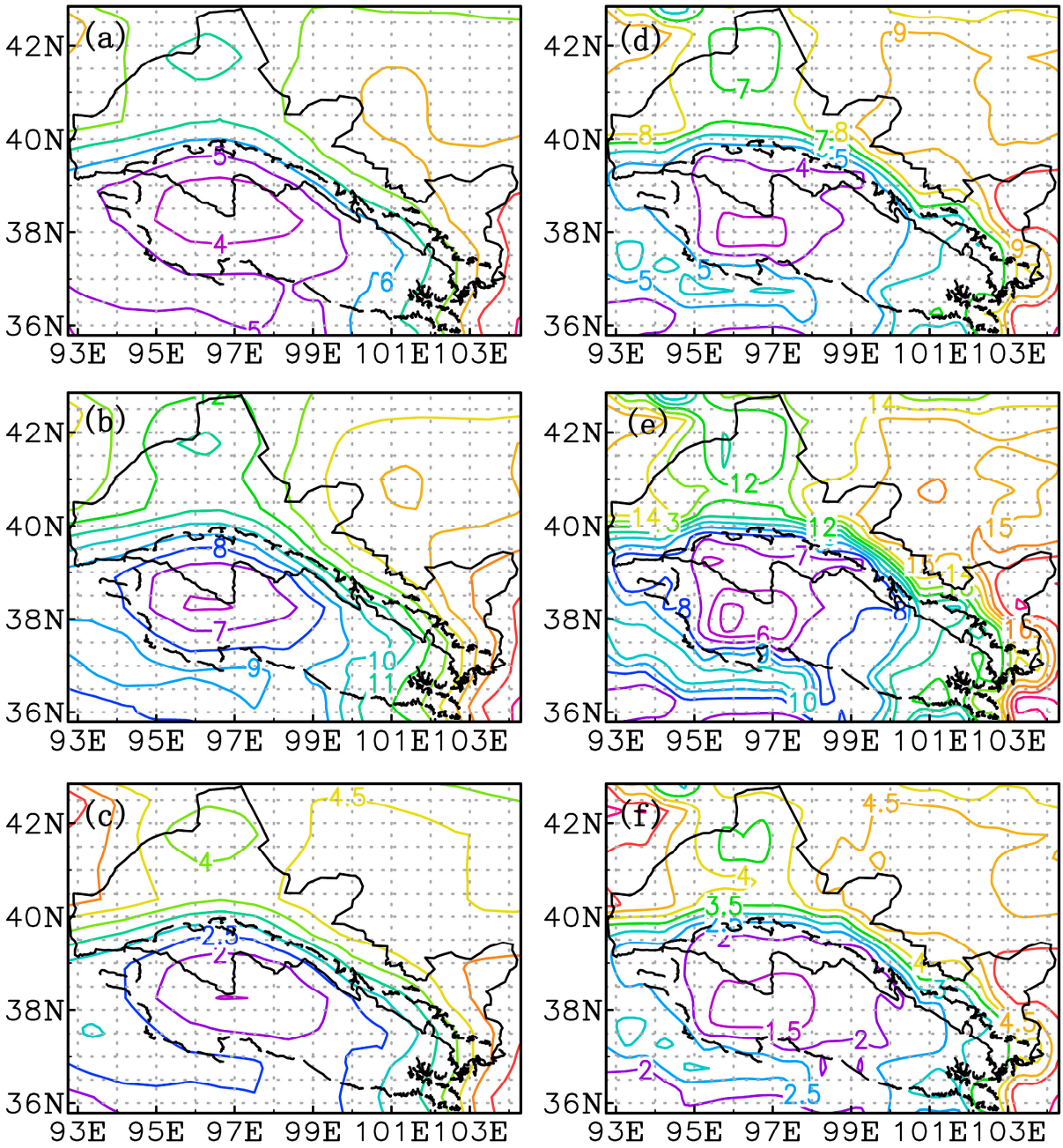

Figure 4. The atmospheric precipitable water content climatology during the annual (**a**,**d**), wet season (**b**,**e**) and dry season (**c**,**f**) from ERA-Interim (**a**–**c**) and MERRA-2 (**d**–**f**) in the QM-HCR.

Water vapor convergence mainly occurs in the central-eastern QMR, the southeast-northwestern HCR, Mazong Mountains, Hami and certain surrounding areas; the convergence is more significant in the wet season. Water vapor divergence mainly occurs in other regions of the QM-HCR annually; it mainly occurs in the QM-HCR, except for the Mazong Mountains, Hami, and certain surrounding areas during the dry season.

There is always a water vapor convergence center in the Hami and the surrounding area (the northwest corner of Figure 5a–c). The yearly average precipitation is only 43.6 mm at the Hami station, indicating the complexity of the precipitation formation process.

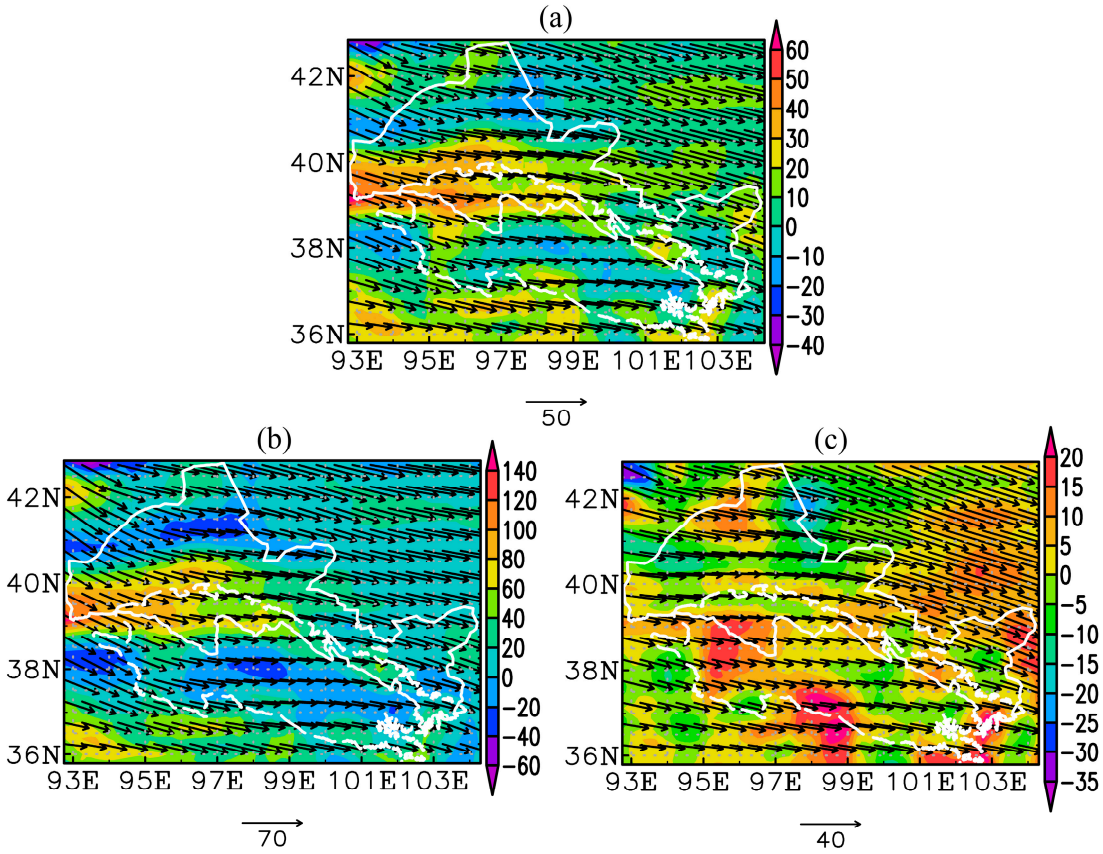

Figure 5. The water vapor flux climatology (units: kg m^{-1} s^{-1}) during the annual (**a**), wet season (**b**) and dry season (**c**) from ERA-Interim, the arrow direction represents the direction of the water vapor flux, the arrow size represents the value of the water vapor flux, and the shade is the water vapor flux divergence (units: 10^{-6} kg m^{-2} s^{-1}).

3.3. Boundary and Regional Net Water Vapor Flux

The annual net water vapor flux in 1980–2017 in the QM-HCR suggests that the flux is 395.65 × 10^6 kg/s, 298.28 × 10^6 kg/s, 72.79 × 10^6 kg/s, and 166.41 × 10^6 kg/s at the eastern, western, southern, and northern boundaries (Figure 6a), respectively. The water vapor flux is 203.07 × 10^6 kg/s, 163.39 × 10^6 kg/s, 41.46 × 10^6 kg/s, and 74.31 × 10^6 kg/s at the eastern, western, southern, and northern boundaries during the wet season (Figure 6b), respectively. Similarly, it is 192.57 × 10^6 kg/s, 134.89 × 10^6 kg/s, 31.33 × 10^6 kg/s, and 92.10 × 10^6 kg/s during the dry season (Figure 6c), respectively.

The regional net water vapor flux is −3.75 × 10^6 kg/s, −6.84 × 10^6 kg/s, and 3.09 × 10^6 kg/s in the QM-HCR annually and during the wet and dry seasons, respectively. Water vapor flux is positive at the western and northern boundaries but negative at the southern and eastern borders. This result indicates that water vapor mainly inputs through the western (approximately 64%) and northern boundaries and mostly outputs through the eastern (approximately 84%) and southern boundaries. Water vapor exhibits a net loss during the annual and wet season but presents a net gain during the dry season.

3.4. Water Vapor Transport between the QMR and the HCR

By dividing the column-integrated air (surface—200 hPa) into the low troposphere (surface—600 hPa), middle troposphere (600–400 hPa), and high troposphere (400–200 hPa), the climatology of the stratified regional net water vapor flux is calculated to investigate the vertical distribution characteristics of water vapor.

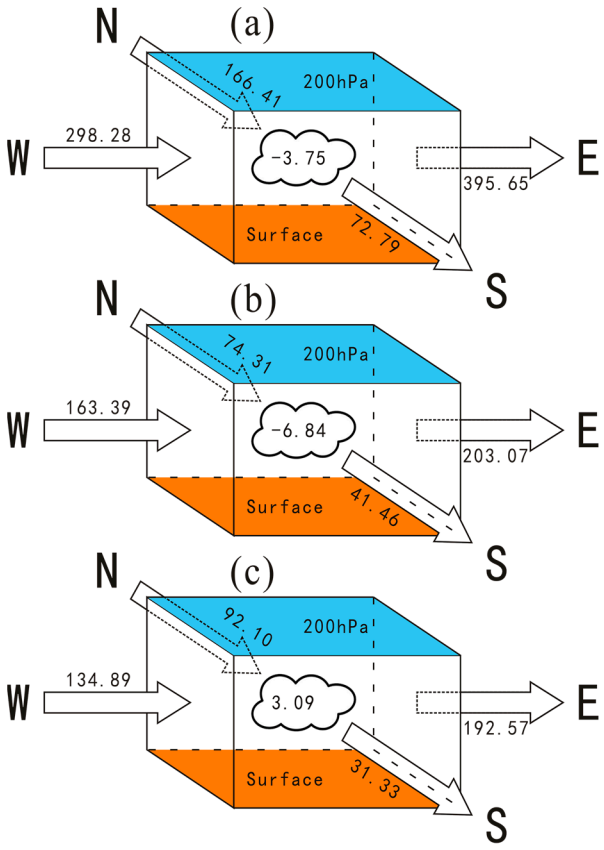

Figure 6. The climatology of boundary and regional net water vapor flux during the annual (**a**), wet season (**b**), and dry season (**c**) by the average between ERA-Interim and MERRA-2 in the QM-HCR.

The proportions of atmospheric PWC are 59.93 ± 1.04%, 34.20 ± 0.88%, and 5.86 ± 0.16% in the low troposphere, middle troposphere, and high troposphere, respectively (Figure 7). Water vapor flux climatology annually and during the wet and dry seasons in the low troposphere suggests that more than 90% of the QMR areas display water vapor convergence in the low troposphere annually (Figure 8a) and during the wet season (Figure 8b). Water vapor convergence centers are in the vicinity of MY, DLH, and the Mazong Mountain Region.

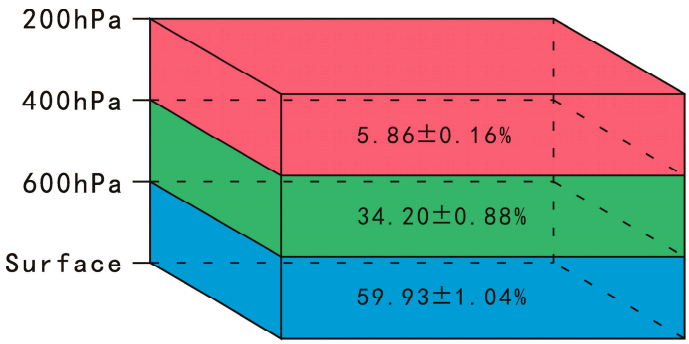

Figure 7. The estimated proportions(percent) of PWC of atmospheric precipitable water content at different pressure levels. The 59.93 ± 1.04%, 34.20 ± 0.88%, and 5.86 ± 0.16% are the average and standard deviation calculated from the average between ERA-Interim and MERRA-2 from 1980 to 2017 in the QM-HCR, respectively.

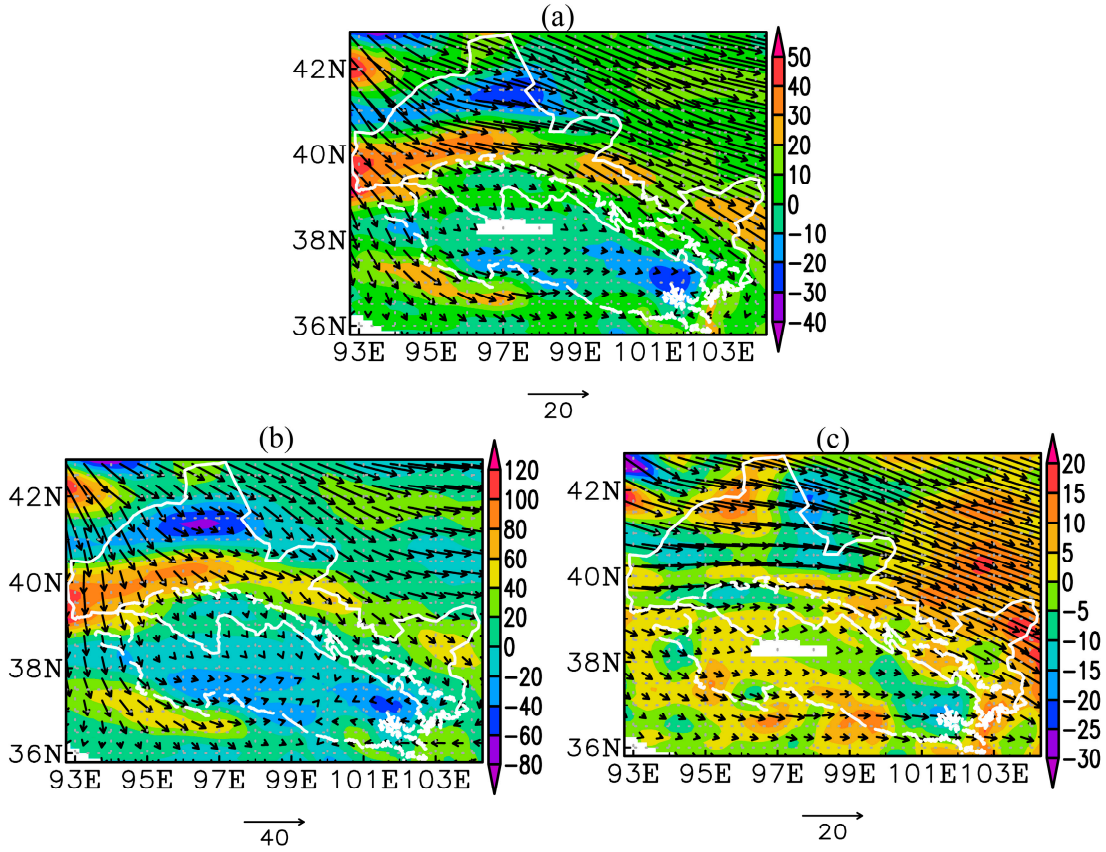

Figure 8. The water vapor flux (units: kg $m^{-1} \cdot s^{-1}$) and water vapor flux divergence (units: 10^{-6} kg·$m^{-2} \cdot s^{-1}$) climatology during the annual (**a**), wet season (**b**) and dry season (**c**) from ERA-Interim in the low troposphere.

Two water vapor transport channels can be identified in the low troposphere of the QM-HCR. One channel allows transport through the HCR to the northern part of the QMR (MY), and another channel allows transport from the northwestern Qaidam Basin to the northern part of the QMR (MY). The water vapor from the two channels is derived from the westerly and northwesterly wind and is separated in the western HCR. The channels then meet again in the vicinity of DLH and MY considering the dynamics of water vapor convergence, eventually leading to more than 200 mm of annual precipitation in the middle and eastern QMR. Water vapor convergence can be observed in the MY and surrounding areas where the annual rainfall can exceed 400 mm. It is worth noting that most of the water vapor flows into the QMR through the water vapor channel in the northern QMR, and only a small amount of water vapor is transported through another channel. The results indicate that a portion of the recycled moisture generated from the evapotranspiration of forest and cropland over the oasis in the HCR is transported to the QMR, contributing to the abundant precipitation in QMR. This finding also indicates that horizontal moisture recycling is probably one of the most important water cycle mechanisms in the endorheic river basins.

In the dry season (Figure 8c), though most of the QM-HCR displays the water vapor divergence in the low troposphere, water vapor convergence is observed in the MY, Mazong Mountain Region, and in HM. In addition, the two small troposphere water vapor channels still exist. However, the difference is that the water vapor that passes through the northern water vapor channel does not input into the QMR, but directly outputs from the QM-HCR, leading to a net loss of external water vapor budget during the dry season (Figure 8c). This finding indicates that regional moisture recycling also plays a vital role in the dry season for precipitation in the QM-HCR.

4. Discussion

4.1. Comparing Water Vapor Variables of the QM-HCR with Previous Studies

The average atmospheric PWC exhibits distinct unimodal features in the QM-HCR. The atmospheric water content decreases from the surrounding areas to the high-altitude mountains in the QM-HCR, which is similar to that of Tianshan Mountain [36] and contrasts with that of Altay Mountain [26]. These results indicate that the atmospheric PWC has a similar seasonal pattern to the precipitation in northwestern China. However, the atmospheric PWC has a strong pattern of spatial heterogeneity, suggesting the necessity of studying water vapor changes on a regional scale.

The westerly and northwesterly winds control the QM-HCR in months with less precipitation, while the westerly, northwesterly, northerly, southerly, and southeasterly winds control the region in months with abundant precipitation. Wang et al. [20] indicated that northerly winds from the Arctic Ocean and the southeast monsoon could reach the QM-HCR in certain months with high precipitation. On combining the above results, it can be concluded that the QM-HCR is mainly affected by the westerly winds, northerly winds, and the southeast monsoon. The "mutual offset" phenomenon of water vapor flux in the air in the QM-HCR can also be found on the Qinghai-Tibetan Plateau [23].

The changes in annual precipitation and water vapor variables are poorly correlated in the QM-HCR (Table 2). Precipitation is positively correlated with water vapor transported by latitudinal winds but negatively correlated with that carried by longitudinal winds (Table 2). The precipitation is positively correlated with water vapor passing through the eastern, western, and southern boundaries but negatively correlated with winds passing through the northern border. A previous study on the relationship between precipitation in QMR and the monsoon index suggested that precipitation is poorly correlated with the East Asian, South Asian, South China Sea monsoons, zonal winds, and subtropical anticyclones [37]. These findings indicate that the precipitation mechanism probably has a strong linkage with local moisture recycling.

Table 2. Pearson Correlation between the observed precipitation, evaporation and boundary and regional net water vapor flux.

Time Scale	Evaporation	Regional	Latitudinal	Longitudinal	East	West	South	North	Total Input	Total Output
annual	0.46 **	0.29	0.39 *	−0.33 *	0.18	0.14	0.26	−0.39 *	−0.19	−0.24
Wet season	0.02	0.38 *	0.32	−0.21	0.12	0.19	0.31	−0.32	−0.13	−0.20
Dry season	0.10	−0.42 **	0.28	−0.40 *	0.08	0.05	0.16	−0.36 *	−0.17	0.11

**: Significant correlation at $\alpha = 0.01$; *: Significant correlation at $\alpha = 0.05$.

4.2. Potential Driving Mechanism of Horizontal Transport of Water Vapor

Analysis of the reanalysis dataset indicates that there are two water vapor transport channels in the low troposphere of the QM-HCR. Most of the water vapor flows into the QMR through the water vapor channel in the northern QMR, which shows that the abundant precipitation in QMR is probably partially generated from the recycled moisture over HCR, partially proving the hypothesis of [17].

The primary driving mechanism of the horizontal transport of recycled moisture can be explained by the significant difference in temperature and humidity between the HCR and the QMR in the QM-HCR. Such a difference is mainly forced by the "cold and wet island effect" of the cryosphere [38] in QMR, where the air temperature of the glacier is cold, and the relative humid is wet, especially during the wet season. Evapotranspiration is very strong in the warm and dry climate across the desert and oasis of the HCR, which provides high amounts of recycled moisture. The cryosphere modifies the temperature and humidity of the underlying surface in the QMR, which leads to lower temperatures in the QMR and lower evapotranspiration. Under the influence of the significant difference of surface temperature between the cryosphere and other land cover types, the recycled moisture

in deserts and oases is transported to the mountains, resulting in an active horizontal turbulent exchange among mountains, deserts, and oases.

The recycled moisture in the low mountains also migrated to the high mountains under the influence of terrain uplift. The horizontal turbulent motions change the temperature convection and increase the atmospheric water vapor over the QMR, leading to more precipitation. The atmospheric transport of hot air from the desert and low mountains to the upper atmosphere in a cold island, probably forms an upper hot and lower cold inversion layer in the QMR, further strengthening the turbulent horizontal movement. The recycled moisture is more affected by the cryospheric condensation and forms precipitation under appropriate atmospheric conditions in the QMR. Although the mechanism appears feasible, more evidence and descriptions are needed in future studies. This transport mechanism requires further analysis on a smaller scale, such as using the coupling WRF (Weather Research and Forecasting) mesoscale model with a distributed hydrological model in the QM-HCR.

The precipitation in the wet season is about 85% of the annual precipitation, thus the water vapor transport channel is more pronounced in the wet season (Figure 8b) and annual (Figure 8a), while it is relatively weak in the dry season (Figure 8c). The QM-HCR is mainly controlled by the westerly wind with less water vapor, so it is relatively more important than recycled moisture in the precipitation. Unfortunately, we cannot provide the exact contribution of this and future study is still needed.

4.3. Long Term Changes in Regional Net Water Vapor Flux

The long-term changes of water vapor flux at each boundary make the input water vapor flux to QM-HCR showed a significant ($\alpha = 0.05$) decrease by 22.2×10^6 kg s^{-1} decade^{-1} and 18.8×10^6 kg s^{-1} decade^{-1}, respectively, while the output water vapor flux has a more significant ($\alpha = 0.01$) reduction by 31.2×10^6 kg s^{-1} decade^{-1} and 28.0×10^6 kg s^{-1} decade^{-1} during annual and wet season, respectively. The regional net water vapor flux shows a significant ($\alpha = 0.01$) increase by 9.1×10^6 kg s^{-1} decade^{-1} and 9.2×10^6 kg s^{-1} decade^{-1}, respectively, which correspond to the significant ($\alpha = 0.05$) increase of precipitation by 7.4 mm/decade and 5.5 mm/decade during annual and wet seasons from 1980 to 2017 in the QM-HCR, respectively. These results indicate that the arid degree tends to decrease in the QM-HCR, and which is consistent with the changes in Northwestern China [39].

During the dry season, all water vapor fluxes have no significant ($\alpha = 0.1$) changes. The water vapor flux is always less than 0 kg s^{-1} at the southern boundary during annual and dry seasons, while it is sometimes greater than 0 kg s^{-1} during the wet season (considering the standard deviation). It suggests that there are some positive water vapor fluxes at the southern boundary only in the wet season, especially during 2003 to2014, which indicates that the Southerly Wind (component) can arrive at the QM-HCR during the wet season in some years and contribute to the local precipitation, while it cannot arrive during the dry season.

The above results suggest that the water vapor flux undergoes intensive change at the eastern and northern boundaries. Although the linear trends of precipitation and regional net water vapor flux are consistent at annual scales, but the fluctuations varied in different years, and the opposite "peak-valley" fluctuations occurred in some years such as in extreme climate years (including drought and humid), which indicates that the local precipitation is affected by many climatic factors in the QM-HCR, such as the surface vorticity, 500 hPa relative humidity, near surface specific humidity, 500 hap divergence, local topography, and some climate events [40]. During annual and wet seasons, the total input and output water vapor flux significantly decreased, and the decrease of the total output water vapor flux is greater than that of the total input water vapor flux, which indicates that the regional moisture recycle is more intensified, and the contribution of recycled moisture variation to precipitation change increased.

4.4. Uncertainty

There are many uncertainties in the observation, reanalysis datasets, and analysis methods used in the study considering the complex terrain and limited field observation data in the QM-HCR.

The in-situ precipitation data of the QM-HCR were mainly obtained from Chinese national meteorological stations. The national meteorological station network is sparse in western China, especially in high mountainous areas. Although some automatic weather stations have been established in QMR in recent years, the observation time-span is not long [7]. This led to an understanding that the temporal and spatial characteristics of precipitation in the QM-HCR have certain limitations and uncertainties.

There is some uncertainty regarding the use of ERA-Interim and MERRA-2 to analyze the climatological patterns of water vapor in the QM-HCR. In general, models cannot represent spatial variability on scales smaller than that defined by the spacing between the discrete points in the grid scale. Models do not represent the grid scale very well either, with the effective resolution of models being somewhat larger than the grid scale. In the horizontal, the ECMWF IFS in addition to using grid points, it also uses an additional mathematical concept, spectral space, to represent horizontal space, which uses a set of wavy basis functions, spherical harmonics, to describe variations in the horizontal. The IFS switches between spectral space and grid space in order to perform specific computations. In the vertical, IFS can use levels located at discrete points, and/or averages over layers. The data collections from MERRA-2 are provided on the same horizontal grid, while the output collections of MERRA-2 are on the regular $0.5^\circ \times 0.625^\circ$ latitude-by-longitude grid, the GEOS-5 model computed all fields on a cubed-sphere grid with an approximate resolution of 50 km $\times$ 50 km. In the vertical, MERRA-2 outputs are provided on either the native vertical grid (at 72 model layers or the 73 edges), or interpolated to 42 standard pressure levels. The varied horizontal and vertical scales lead to it being difficult to evaluate the impact of the resolution on the accuracy of water flux, which probably leads to more uncertainties.

ERA-Interim and MERRA-2 are reanalysis datasets with similar model structures and assimilation schemes, which may lead to common systematic errors [26,32]. There are substantial differences between the two datasets given the inherent uncertainties of the forecast model and the input and assimilation data. The uncertainty of a single reanalysis dataset may be reduced by combining different reanalysis datasets, which will likely help in comprehensive analyses and the extraction of more realistic features [41]. However, there are probably other methods to use for reanalysis datasets that can also reduce uncertainty.

There are also some uncertainties involved in the method we used to calculate water vapor transport. When calculating the boundary and regional net water vapor flux, we only considered the minimum envelope rectangle of the QM-HCR, that is, the eastern, western, southern, and northern boundaries; these are not distinctly defined [42]. The relationship between external water vapor, recycled moisture, and observed precipitation was calculated using the Pearson Correlation method, which has some uncertainties. We identified two channels in the low troposphere (surface—600 hPa) transport water vapor from the HCR to the QMR in this study, which partly explain the mechanism of abundant precipitation in QMR. However, considering that the mechanism is complex and difficult to observe, more evidence is needed for validation.

Generally, there are many uncertainties regarding water vapor transport because of the difficulties involved in large-scale observation of the process. In our study, water vapor transport was calculated using reanalysis datasets. We were unable to validate our results using other observations or models. Isotope tracing, WRF and Hysplit tracing models, and the Lagrangian approach can be used to verify and analyze the external water vapor and recycled moisture transport process during different time scales in the QM-HCR. However, these methods also have some deficiencies when applied individually. There is still a need for integrated research on water vapor transport using different observation methods.

5. Conclusions

The climatological patterns of water vapor in the QM-HCR were investigated by the monthly ERA-Interim and MERRA-2 in 1980–2017, providing important implications for the horizontal transport of recycled moisture. The following significant conclusions can be drawn:

(1) Two channels identified transport water vapor from the arid HCR to the QMR in the low troposphere (surface–600 hPa), suggesting that parts of recycled moisture generated from evapotranspiration over the oasis and desert of the HCR are transported to the QMR, which contributes to the abundant precipitation in the QMR.

(2) The primary driving mechanism of the horizontal transport of recycled moisture may be led by the significant difference in temperature and humidity between the HCR and the QMR, caused by the "cold and wet island effect" of the cryosphere in QMR, especially during the wet season.

(3) The water vapor transport from HCR to QMR indicates that horizontal moisture recycling is probably an essential mechanism of the water cycle in endorheic river basins, where water resources are mainly generated from mountainous areas.

Author Contributions: Conceptualization, Z.Z. and S.Z.; Methodology, Z.Z.; Software, Q.Z. and Z.Z.; Validation, Q.Z. and S.Z.; Formal Analysis, S.Z.; Investigation, S.Z. and Z.Z.; Resources, S.Z.; Data Curation, Q.Z.; Writing—Original Draft Preparation, Z.Z. and S.Z.; Writing—Review & Editing, S.Z.; Visualization, Q.Z. and Z.Z.; Supervision, S.Z.; Project Administration, S.Z.; Funding Acquisition, S.Z. All authors have read and agreed to the published version of the manuscript.

Funding: This work was supported by the National Natural Science Foundation of China (41730751).

Data Availability Statement: All relevant data can be obtained from the following links. ERA-Interim can be obtained from https://www.ecmwf.int/en/forecasts/dataset/ecmwf-reanalysis-interim (accessed on 10 September 2020), MERRA-2 from https://disc.gsfc.nasa.gov (accessed on 12 October 2018), and observed monthly precipitation data from http://data.cma.cn (accessed on 12 October 2018).

Acknowledgments: Thanks to three anonymous referees for their helpful suggestions, which significantly improved the quality of the manuscript.

Conflicts of Interest: The authors declare no conflict of interest. The founding sponsors had no role in the design of the study; in the collection, analyses, or interpretation of data; in the writing of the manuscript; or in the decision to publish the results.

References

1. Huang, P.; Yu, H.P.; Guan, X.D.; Wang, G.Y.; Guo, R.X. Accelerated dryland expansion under climate change. *Nat. Clim. Chang.* **2016**, *6*, 166–171. [CrossRef]
2. Xia, J.; Ning, L.; Wang, Q.; Chen, J.X.; Wan, L.; Hong, S. Vulnerability of and risk to water resources in arid and semi-arid regions of West China under a scenario of climate change. *Clim. Chang.* **2017**, *144*, 549–563. [CrossRef]
3. Rotenberg, E.; Yakir, D. Contribution of semi-arid forests to the climate system. *Science* **2010**, *327*, 451–454. [CrossRef] [PubMed]
4. Wang, L.; Chen, R.S.; Han, C.T.; Wang, X.Q.; Liu, G.H.; Song, Y.X.; Yang, Y.; Liu, J.F.; Liu, Z.W.; Liu, X.J.; et al. Change characteristics of precipitation and temperature in the Qilian Mountains and Hexi Oasis, Northwestern China. *Environ. Earth Sci.* **2019**, *78*, 284. [CrossRef]
5. Wang, N.L.; Zhang, S.B.; He, J.Q.; Pu, J.C.; Wu, X.B.; Jiang, X. Tracing the major source area of the mountainous runoff generation of the Heihe River in northwest China using stable isotope technique. *Chin. Sci. Bull.* **2009**, *54*, 2751–2757. (In Chinese with English abstract) [CrossRef]
6. Chen, R.S.; Han, C.T. Hydrology, Ecology and Climate Significance and Its Research Progress of the Alpine Cold Desert. *Adv. Earth Sci.* **2010**, *25*, 255–263. (In Chinese with English abstract) [CrossRef]
7. Zhang, Z.H.; Deng, S.F.; Zhao, Q.D.; Zhang, S.Q.; Zhang, X.W. Projected glacier meltwater and river run-off changes in the Upper Reach of the Shule River Basin, north-eastern edge of the Tibetan Plateau. *Hydrol. Process.* **2019**, *33*, 1059–1074. [CrossRef]
8. He, Z.B.; Zhao, W.Z.; Liu, H.; Tang, Z.X. Effect of forest on annual water yield in the mountains of an arid inland river basin: A case study in the Pailugou catchment on northwestern China's Qilian Mountains. *Hydrol. Process.* **2012**, *26*, 613–621. [CrossRef]
9. Gao, Q.Z.; Du, H.L.; Zu, R.P. The balance between supply and demand of water resources and the water-saving potential for agriculture in the Hexi Corridor. *Chin. Geogr. Sci.* **2002**, *12*, 23–29. [CrossRef]
10. Held, I.M.; Soden, B.J. Water vapor feedback and global warming. *Annu. Rev. Energy Environ.* **2000**, *25*, 441–475. [CrossRef]

11. Hubert, H.S. New definitions for moisture recycling and the relationship with land-use changes in the Sahel. *J. Hydrol.* **1995**, *167*, 57–78.
12. Ma, Y.; Lu, M.; Chen, H.; Pan, M.; Hong, Y. Atmospheric moisture transport versus precipitation across the Tibetan Plateau: A mini-review and current challenges. *Atmos. Res.* **2018**, *209*, 50–58. [CrossRef]
13. Chen, B.; Xu, X.D.; Yang, S.; Zhang, W. On the origin and destination of atmospheric moisture and air mass over the Tibetan Plateau. *Theor. Appl. Climatol.* **2012**, *110*, 423–435. [CrossRef]
14. Zhang, C.; Tang, Q.; Chen, D. Recent changes in the moisture source of precipitation over the Tibetan Plateau. *J. Clim.* **2017**, *30*, 1807–1819. [CrossRef]
15. Ma, Y.; Lu, M.; Bracken, C.; Chen, H. Spatially coherent clusters of summer precipitation extremes in the Tibetan Plateau: Where is the moisture from? *Atmos. Res.* **2020**, *237*, 104841. [CrossRef]
16. Zhao, L.J.; Liu, X.H.; Wang, N.L.; Kong, Y.L.; Song, Y.X.; He, Z.B.; Liu, Q.Y.; Wang, L.X. Contribution of recycled moisture to local precipitation in the inland Heihe River Basin. *Agric. For. Meteorol.* **2019**, *271*, 316–335. [CrossRef]
17. Ding, Y.J.; Zhang, S.Q. Study on Water Internal Recycle Process and Mechanism in Typical Mountain Areas of Inland Basins, Northwest China: Progress and Challenge. *Adv. Earth Sci.* **2018**, *33*, 719–727. (In Chinese with English abstract) [CrossRef]
18. Liu, G.W. *Atmospheric Processes of Hydrological Cycle*; Science Press: Beijing, China, 1997. (In Chinese)
19. Saha, S.; Moorthi, S.; Pan, H.L.; Wu, X.R.; Wang, J.D.; Nadiga, S.; Tripp, P.; Kistler, R.; Woollen, J.; Behringer, D.; et al. The NCEP Climate Forecast System Reanalysis. *Bull. Am. Meteorol. Soc.* **2010**, *91*, 1015–1058. [CrossRef]
20. Wang, X.J.; Pang, G.J.; Yang, M.X.; Wan, G.N.; Liu, Z.C. Precipitation changes in the Qilian Mountains associated with the shifts of regional atmospheric water vapor during 1960–2014. *Int. J. Climatol.* **2018**, *38*, 4355–4368. [CrossRef]
21. Simmons, A.J.; Willett, K.M.; Jones, P.D.; Thorne, P.W.; Dee, D.P. Low-frequency variations in surface atmospheric humidity, temperature and precipitation: Inferences from reanalyses and monthly gridded observational datasets. *J. Geophys. Res.* **2010**, *115*, 1–21. [CrossRef]
22. Decker, M.; Brunke, M.A.; Wang, Z.; Sakaguchi, K.; Zeng, X.; Bosilovich, M.G. Evaluation of the reanalysis products from GSFC, NCEP, and ECMWF Using Flux Tower Observations. *J. Clim.* **2012**, *25*, 1916–1944. [CrossRef]
23. Xie, X.R.; You, Q.L.; Bao, Y.T.; Meng, X.H. The Connection Between the Precipitation and Water Vapor Transport over Qinghai-Tibetan Plateau in Summer Based on the Multiple Datasets. *Plateau Meteorol.* **2018**, *37*, 78–92. (In Chinese with English abstract) [CrossRef]
24. Jiang, J.; Zhou, T.J.; Zhang, W.X. Evaluation of Satellite and Reanalysis Precipitable Water Vapor Data Sets Against Radiosonde Observations in Central Asia. *Earth Space Sci.* **2019**, *6*, 1129–1148. [CrossRef]
25. Gelaro, R.; Mccarty, W.; Suárez, M.J.; Todling, R.; Molod, A.; Takacs, L.; Radles, C.A.; Darmenov, A.; Bosilovich, M.G.; Reichle, R. The Modern-Era Retrospective Analysis for Research and Applications, Version 2 (MERRA-2). *J. Clim.* **2017**, *30*, 5419–5454. [CrossRef] [PubMed]
26. Li, S.; Xie, G.H.; He, Q.; Li, X.Y. Research on Precipitation, Precipitable Water and the Precipitation Conversion Efficiency of Altay Prefecture. *J. Glaciol. Geocryol.* **2008**, *30*, 675–680. (In Chinese with English abstract)
27. Yao, J.Q.; Chen, Y.N.; Yang, Q. Spatial and temporal variability of water vapor pressure in the arid region of northwest China, during 1961–2011. *Theor. Appl. Climatol.* **2016**, *123*, 683–691. [CrossRef]
28. Chow, K.C.; Tong, H.W.; Chan, J.C.L. Water vapor sources associated with the early summer precipitation over China. *Clim. Dyn.* **2008**, *30*, 497–517. [CrossRef]
29. Meng, X.J.; Zhang, S.F.; Zhang, Y.Y.; Wang, C.C. Temporal and spatial changes of temperature and precipitation in Hexi Corridor during 1955–2011. *J. Geogr. Sci.* **2013**, *23*, 653–667. [CrossRef]
30. Oliver, M.A.; Webster, R. Kriging: A method of interpolation for geographical information systems. *Int. J. Geogr. Inf. Syst.* **1990**, *4*, 313–332. [CrossRef]
31. Miao, Q.J.; Xu, X.D.; Zhang, S.Y. Whole layer water vapor budget of Yangtze River valley and moisture flux components transform in the key areas of the plateau. *Acta Meteorol. Sin.* **2005**, *63*, 93–99. (In Chinese with English abstract) [CrossRef]
32. Dee, D.P.; Uppala, S.M.; Simmons, A.J.; Berrisford, P.; Poli, P.K.; Kobayashi, S.; Andrae, U.; Balmaseda, M.A.; Balsamo, G.; Bauer, P. The ERA-Interim reanalysis: Configuration and performance of the data assimilation system. *Q. J. R. Meteorol. Soc.* **2011**, *137*, 553–597. [CrossRef]
33. Trenberth, K.E. Climate Diagnostics from Global Analyses: Conservation of Mass in ECMWF Analyses. *J. Clim.* **1991**, *4*, 707–722. [CrossRef]
34. Zhou, T.J. Comparison of the global air-sea freshwater exchange evaluated from independent datasets. *Prog. Nat. Sci.* **2003**, *13*, 626–631.
35. Wang, K.L.; Cheng, G.D.; Xiao, H.L.; Jiang, H. The westerly fluctuation and water vapor transport over the Qilian-Heihe valley. *Sci. China Ser. D Earth Sci.* **2004**, *47*, 32–38. [CrossRef]
36. Li, X.; Zhang, G.X. Research on Precipitable Water and Precipitation Conversion Efficiency around Tianshan Mountain Area. *J. Desert Res.* **2003**, *23*, 509–513. (In Chinese with English abstract) [CrossRef]
37. Zhang, L.; Zhang, Q.; Feng, J.Y.; Bai, H.Z.; Zhao, J.H.; Xu, X.H. A study of atmospheric water cycle over the Qilian Mountains (I): Variation of annual water vapor transport. *J. Glaciol. Geocryol.* **2014**, *36*, 1079–1091. (In Chinese with English abstract) [CrossRef]
38. Chen, R.S.; Han, C.T.; Liu, J.F.; Yang, Y.; Liu, Z.W.; Wang, L.; Kang, E.S. Maximum precipitation altitude on the northern flank of the Qilian Mountains, northwest China. *Hydrol. Res.* **2018**, *49*, 1696–1710. [CrossRef]

39. Peng, D.D.; Zhou, T.J. Why was the arid and semiarid northwest China getting wetter in the recent decades? *J. Geophys. Res.* **2017**, *122*, 9060–9075. [CrossRef]
40. Yang, C.L.; Wang, N.L.; Wang, S.J. A comparison of three predictor selection methods for statistical downscaling. *Int. J. Climatol.* **2017**, *37*, 1238–1249. [CrossRef]
41. Sun, Q.H.; Miao, C.Y.; Duan, Q.Y.; Ashouri, H.; Sorooshian, S.; Hsu, K.L. A review of global precipitation data sets: Data sources, estimation, and intercomparisons. *Rev. Geophys.* **2018**, *56*, 79–107. [CrossRef]
42. Guan, X.F.; Mei, Y.L.; Xie, Z.Y.; Gang, L.J. Spatial distribution, temporal variation, and transport characteristics of atmospheric water vapor over Central Asia and the arid region of China. *Glob. Planet. Chang.* **2018**, *172*, 159–178. [CrossRef]